


Estimating angoricity and granular equations of state for monodisperse packings of frictional hard spheres in a wide range of densities

Vasili Baranau* and Ulrich Tallarek 

Department of Chemistry, Philipps-Universität Marburg, 35032 Marburg, Germany



(Received 9 September 2023; accepted 19 March 2024; published 18 April 2024)

In this paper, we study the granular equation of state (EOS) for computer-generated three-dimensional mechanically stable packings of frictional monodisperse particles over a wide range of densities (packing fractions), $\varphi = 0.56\text{--}0.72$. As a statistical physics framework, we utilize the statistical ensemble for granular matter, specifically the “angoricity” ensemble, where the compressional component Σ_p of the force-moment tensor serves as granular energy and angoricity A_p is the corresponding granular “temperature.” We demonstrate that the systems under study conform well to this statistical description, and the simple equation of state $\Sigma_p = 2.8NA_p$ holds very well, where N is the number of particles. We show that granular temperature exhibits a rapid drop around the random-close packing (RCP) limit $\varphi \approx 0.64\text{--}0.65$, and, hence, one can say that granular packings “freeze” at the RCP limit. We repeat these calculation for shear angoricity A_{sh} and shear component Σ_{sh} of the force-moment tensor and obtain a similar EOS, $\Sigma_{sh} = 0.85NA_{sh}$. Additionally, we measure the so-called keramicity, an inverse temperature variable corresponding to the determinant of the force-moment tensor, while pressure angoricity corresponds to its trace. We show that inverse keramicity κ^{-1} and angoricity A_p conform to an EOS $\frac{1}{A_p} \frac{\Sigma_p}{N} + 0.11\kappa \left(\frac{\Sigma_p}{N}\right)^3 = 1.2$, whose form is predicted by mean-field theory. Finally, we demonstrate that the alternative statistical ensemble where Voronoi volumes serve as granular energy (and so-called compactivity serves as temperature) does not describe the systems under study well.

DOI: [10.1103/PhysRevE.109.044904](https://doi.org/10.1103/PhysRevE.109.044904)

I. INTRODUCTION

Granular media are ubiquitous in nature and industrial applications: sand, grains, avalanches, and formation of asteroids and planets are just some examples of granular matter and granular phenomena. As much as statistical physics for usual thermal matter is helpful in understanding thermodynamics and chemistry of the thermal matter, so much (it is hoped) statistical physics for granular matter will help uncover the secrets of the latter and explain its behavior. For example, such a theory can lead to better understanding of avalanches and earthquakes and help create better early detection systems for these natural disasters.

In recent years, a model for statistical physics of granular matter has emerged [1,2]. It treats the trace of the force-moment tensor as granular energy and defines the corresponding intensive temperature-like variable called “angoricity.” Another version of this framework uses Voronoi volumes (more precisely, set Voronoi volumes) around particles as granular energy, while the corresponding temperature variable is called “compactivity.”

Collections of hard spheres is a popular model in granular and glass physics to investigate dynamical and static properties of granular and glassy systems. Thermal hard-sphere systems are characterized by a single parameter—particle volume fraction (packing density)—while thermodynamic temperature can be set to an arbitrary value by rescaling the

unit of time. At the same time, they are versatile enough to reproduce multitude of phenomena such as the random-close packing (RCP) limit, melting and freezing transitions, glass transition, and others [3,4].

In this work, we apply and verify the statistical mechanics framework of granular matter to computer-generated mechanically stable isotropic systems of three-dimensional frictional hard spheres in a wide range of packing densities and demonstrate that the statistical ensemble based on angoricity seems to better describe the systems under study than the ensemble based on compactivity.

A. Related work

The work on hard-sphere systems as a model of granular media spans decades and is closely related to a large body of work on thermal hard-sphere systems (as a model of colloids and glasses), and it is impossible to cover it concisely. For some recent reviews, see Refs. [1,2]. For this paper, the following works are the most relevant.

Works of Edwards and coauthors established a foundation for treating granular systems statistically and introduced the concepts of the Edwards entropy, compactivity and angoricity, as well as the assumption that all granular packings in the microcanonical ensemble are equiprobable [5,6]. Works of Henkes and Chakraborty and coauthors [7] refined and extended these concepts. For example, Eq. (23) in Ref. [7] is an equation of state (EOS) for granular matter derived theoretically in the mean-field limit for frictionless spheres, on which we rely further. Reference [8] provides a phase

*vasili.baranov@gmail.com

diagram for the jammed matter which includes the coordination number, packing density, and compactivity as coordinates. It does not include angoricity, though. Reference [9] measures angoricity and compactivity of three-dimensional (3D) spheres without friction. In the present work, we measure angoricity and compactivity for 3D spheres with friction. Reference [10] measures angoricity and compactivity for 2D frictional disks using the method of overlapping histograms and the method based on the fluctuation-dissipation theorem (FDT). The present paper extends this work to 3D frictional spheres. A more recent work [11] also focuses on 2D frictional disks but analyzes one more inverse temperature-like variable, keramicity. Under certain assumptions, this variable corresponds to higher-order terms in log-differences of overlapping histograms, while angoricity corresponds to the linear term. In general, keramicity is a variable reciprocal to the determinant of the force-moment tensor, which in 2D corresponds to the “Maxwell-Cremona force-tile area” and in 3D to the “Beltrami volume” [12,13]. We estimate keramicity for the systems under study as well, for the first time, to the best of our knowledge, for 3D systems. Reference [12] conducts careful computer simulations to study angoricity, keramicity, and finite-size effects for 2D systems. Reference [13] provides a mean-field theory for granular matter and constructs a framework for angoricity, keramicity, and a combined EOS from first principles. Reference [14] conducts experiments with frictional 3D packings but estimates compactivity only.

B. Contributions

The present paper provides the following contributions:

(i) We measure for the first time, to the best of our knowledge, pressure and shear angoricity of three-dimensional frictional hard-sphere packings in a wide range of packing densities. We demonstrate that a linear EOS applies.

(ii) Similarly, for the first time, to the best of our knowledge, we estimate keramicity and its EOS for 3D hard spheres in a wide range of densities.

(iii) We demonstrate that compactivity seems to be an inferior candidate for temperature in granular systems than angoricity and keramicity

(iv) We provide a unique view on the “RCP limit” in frictional systems. The “RCP limit” can be interpreted as a phase transition at which granular temperature drops to zero, i.e., granular systems “freeze.”

The paper is structured as follows: In Sec. II, we present a minimal theory for statistical physics of granular matter. Section III gives a short introduction to the method of overlapping histograms used to measure granular temperatures. In Sec. IV, we give an overview of computer simulations to generate the data under study. Section V presents the results and analysis of calculating different versions of granular temperature in the systems under study. Section VI contains summary and conclusions.

II. THEORY

A. Canonical ensemble of granular matter

In this section, we follow Refs. [1,2,5,7,10]. To apply statistical physics to granular matter, we need to define the

internal energy of the system as well as external parameters. One approach is to use system volume V as the granular equivalent of the internal energy, which makes the corresponding intensive variable compactivity X the granular analog of the temperature: $\frac{1}{X} = \frac{\partial S}{\partial V}$. Another approach is to use the force-moment tensor for the granular energy,

$$\hat{\Sigma} = \sum_{i,j} \vec{r}_{ij} \otimes \vec{f}_{ij}, \quad (1)$$

where \otimes denotes the Kronecker (tensor) product and the sum is taken over all (touching) particle pairs of the system of N particles, \vec{r}_{ij} is the vector pointing from the center of particle i to the point of contact with the j th particle, and \vec{f}_{ij} is the interparticle contact force. The force-moment tensor can be expressed through the Cauchy stress tensor $\hat{\sigma}$: $\hat{\Sigma} = V\hat{\sigma}$. The so-called inverse angoricity tensor $\hat{\alpha}$ corresponds then to the inverse temperature: $\hat{\alpha} = \frac{\partial S}{\partial \hat{\Sigma}}$. We note that some papers (e.g., Refs. [9,10]) refer to this variable as to “inverse angoricity” while others [1,7] call it simply angoricity. We will use A for angoricity and $\hat{\alpha}$ for inverse angoricity. We note that $\hat{\alpha}$ corresponds to T^{-1} .

The canonical ensemble for static granular media (the system itself and the “heat” bath) comprises a granular subpacking under study that is part of a bigger mechanically stable packing (bath).

Recent results suggest that compactivity is not equilibrated between a small subsystem and a large bath that surrounds the subsystem, while angoricity is actually equilibrated [10].

In general, forces acting between particles in mechanically stable configurations may be history dependent. Thus, we have to include the forces into the phase space. The partition function for granular media in the angoricity ensemble—if we do not include V into internal energy and treat it as an external parameter—looks like

$$Z_N = \frac{1}{N!} \int_V \cdots \int_V \int_{\vec{f}_{ij}} \Theta_N(\vec{r}_i, \vec{f}_{ij}) e^{-\hat{\alpha}:\hat{\Sigma}} d\vec{r}_1 \cdots d\vec{r}_N d\vec{f}_{ij}, \quad (2)$$

where $\hat{\alpha}:\hat{\Sigma} = \sum_{i,j} \hat{\alpha}_{ij} \hat{\Sigma}_{ij}$ and $\Theta_N(\vec{r}_i, \vec{f}_{ij})$ denotes the delta function that equals infinity when the conditions of valid particle contacts (i.e., the absence of intersections in case of rigid grains) and mechanical stability (force and torque balance) are satisfied and equals zero otherwise.

For isotropic systems, one can simplify treatment of angoricity. For such systems, the external stress that acts on the system in the microcanonical ensemble, as well as the external stress that acts on the bath plus subsystem in the canonical ensemble, are by definition also isotropic. It allows us to describe granular energy by a single parameter, the compressional component of the force-moment tensor,

$$\Sigma_p = (\Sigma_1 + \Sigma_2 + \Sigma_3)/3 = \text{Tr} \hat{\Sigma}/3, \quad (3)$$

where Σ_i are the eigenvalues of $\hat{\Sigma}$ and Tr is the trace. The trace of the force-moment tensor is the hydrostatic pressure multiplied by system volume and is commonly referred to as Γ . Thus, $\Sigma_p = \Gamma/3$. By combining Eqs. (1) and (3) we get

$$\Sigma_p = \frac{1}{3} \sum_{i,j} \vec{r}_{ij} \cdot \vec{f}_{ij}. \quad (4)$$

The reciprocal variable of the compressional component is the scalar inverse “pressure angoricity” (as referred to in Ref. [10]),

$$\alpha_p = \frac{\partial S}{\partial \Sigma_p}. \quad (5)$$

For isotropic systems, as argued in Ref. [7], $\hat{\alpha} = \alpha \hat{I}$, where \hat{I} is the identity matrix. For such systems, $\hat{\alpha} : \hat{\Sigma} = \alpha \Gamma = 3\alpha \Sigma_p = \alpha_p \Sigma_p$ and $\alpha_p = 3\alpha$. The “pressure angoricity” and angoricity are in turn

$$A_p = \frac{1}{\alpha_p}, \quad A = \frac{1}{\alpha} = 3A_p. \quad (6)$$

Thus, we finally write

$$\begin{aligned} Z_N &= \frac{1}{N!} \int_V \dots \int_V \int_{\vec{f}_{ij}} \Theta_N(\vec{r}_i, \vec{f}_{ij}) e^{-\frac{\Sigma_p}{\lambda_p}} d\vec{r}_1 \dots d\vec{r}_N \\ &= \frac{1}{N!} \int_V \dots \int_V \int_{\vec{f}_{ij}} \Theta_N(\vec{r}_i, \vec{f}_{ij}) e^{-\frac{\Gamma}{\lambda}} d\vec{r}_1 \dots d\vec{r}_N. \end{aligned} \quad (7)$$

If we utilize packing volume as granular energy, then the partition function (denoted here as Z_N^χ to distinguish from Z_N above) can be written as

$$Z_N^\chi = \frac{1}{N!} \int_V \dots \int_V \int_{\vec{f}_{ij}} \Theta_N(\vec{r}_i, \vec{f}_{ij}) e^{-\frac{V}{\chi}} d\vec{r}_1 \dots d\vec{r}_N. \quad (8)$$

The volume of a subsystem can be calculated using so-called set (also called radical) Voronoi tessellation. For monodisperse particles, radical Voronoi tessellation is equivalent to a point Voronoi tessellation, so we omit the “radical” below.

One can include both compactivity and angoricity into the partition function, see Eq. (15) in Ref. [1]:

$$Z_N^{p,\chi} = \frac{1}{N!} \int_V \dots \int_V \int_{\vec{f}_{ij}} \Theta_N(\vec{r}_i, \vec{f}_{ij}) e^{-\frac{V}{\chi} - \frac{\Sigma_p}{\lambda_p}} d\vec{r}_1 \dots d\vec{r}_N. \quad (9)$$

We denote this version as $Z_N^{p,\chi}$ to differentiate from the versions from Eqs. (7) and (8) above. Existing reports [10] demonstrate for frictional 2D packings that compactivity does not seem to equilibrate in granular systems (between a “thermostat” and a subsystem). We also demonstrate below that compactivity seems to serve the role of granular temperature worse than angoricity and keramicity (discussed in detail in Sec. VD below).

B. Shear angoricity

Besides pressure angoricity introduced above, one can also measure shear angoricity based on the shear component of the force-moment tensor [1,10]. In 2D systems, the shear component of the force-moment tensor is written as $\Sigma_{\text{sh}} = (\Sigma_1 - \Sigma_2)/2$, given that eigenvalues Σ_1 and Σ_2 are sorted in descending order [1,10].

To extend this quantity to three dimensions, we temporarily switch for convenience to the stress tensor $\hat{\sigma} = \hat{\Sigma}/V$. At a given point, the stress acting on a plane with the normal \vec{n} is $\vec{t} = \hat{\sigma} \vec{n}$. The normal stress acting on this plane is $t_N(\vec{n}) = \vec{t} \cdot \vec{n} = (\hat{\sigma} \vec{n}) \cdot \vec{n}$ while the shear stress for this plane is $t_{\text{sh}} = \|\vec{t} - t_N \vec{n}\|$ (cf. Eq. (3.4.7) in Ref. [15]).

It can be shown that the maximum shear stress in two dimensions (meaning maximum over \vec{n}) is exactly $\sigma_{\text{sh}} =$

$(\sigma_1 - \sigma_2)/2$. In three dimensions, the maximum shear stress is $\sigma_{\text{sh}} = (\sigma_1 - \sigma_3)/2$ (cf. Eq. (3.14.6) in Ref. [15]). Hence, we use

$$\Sigma_{\text{sh}} = (\Sigma_1 - \Sigma_3)/2 \quad (10)$$

as the extension of shear component of the force-moment tensor to 3D and denote the corresponding shear angoricity as A_{sh} .

It is also possible to extend the concept of shear angoricity to 3D using the root-mean-square value of shear stress. One can show (e.g., with the help of a symbolic mathematics package) that the root mean square of shear stress in 2D (assuming averaging over directions of \vec{n}) is $\sigma_{\text{sh,rms}} = \langle t_{\text{sh}} \rangle = (\sigma_1 - \sigma_2)/(2\sqrt{2})$, i.e., proportional to the maximum shear stress. Integration in 3D leads to a more complex result, $\sigma_{\text{sh,rms}}^2 = \frac{2}{15}[(\sigma_1 - \sigma_2)^2 + (\sigma_2 - \sigma_3)(\sigma_1 - \sigma_3)]$, which transforms to the equivalent shear force-moment tensor

$$\Sigma_{\text{sh,rms}}^2 = \frac{2}{15}[(\Sigma_1 - \Sigma_2)^2 + (\Sigma_2 - \Sigma_3)(\Sigma_1 - \Sigma_3)]. \quad (11)$$

Both Eqs. (10) and (11) turn out to have a very similar EOS, so we focus on Eq. (10) in the remainder of this work. Here we denote the corresponding shear angoricity with A_{sh} .

III. METHODS: CALCULATING ANGORICITY AND COMPACTIVITY

To determine granular temperatures (whether it is angoricity or compactivity), we use the overlapping histograms method introduced in Ref. [16] and utilized in Refs. [10,11,17]. Reference [17] demonstrates that the overlapping histograms method and the method based on volume fluctuations and the FDT produce consistent results for compactivity in 2D packings, while compactivities measured through fitting Gamma distributions and through quadron tessellations have incompatible values. Thus, we utilize the method of overlapping histograms below.

The idea of the method of overlapping histograms is to analyze differences in distributions of granular energies. We use the pressure angoricity ensemble as an example in this section. Under the assumption of Boltzmann-like probability distributions, the probability density P to find a subsystem in the canonical ensemble at a granular energy Σ_p shall follow the Boltzmann distribution,

$$P(\Sigma_p, A_p) = \frac{\Omega(\Sigma_p)}{Z_N(A_p)} e^{-\frac{\Sigma_p}{A_p}}, \quad (12)$$

where $\Omega(\Sigma_p)$ is the density of states and $Z_N(A_p)$ is the partition function.

Although the density of states and the partition function may be unknown for a given granular system, it is observed that $\Omega(\Sigma_p)$ is identical for the same granular system under different conditions [10,17]. Thus, for two different preparation protocols labeled 1 and 2, the ratio of the distributions is

$$\frac{P(\Sigma_p, A_{p1})}{P(\Sigma_p, A_{p2})} = \frac{Z_N(A_{p2})}{Z_N(A_{p1})} e^{-(\frac{1}{A_{p1}} - \frac{1}{A_{p2}})\Sigma_p}. \quad (13)$$

If one takes the logarithm of the equation, then it is possible to fit the logarithm of the ratio with a linear fit and determine the slope $\frac{1}{A_{p1}} - \frac{1}{A_{p2}}$, thus measuring the difference of inverse

temperatures. This procedure allows measuring inverse temperatures up to a specific constant, $\frac{1}{A_p} - C_{A,p}$. By fitting $C_{A,p}$, one can determine final values of A_p . Same considerations apply to shear angoricity and compactivity ensembles. For the shear angoricity ensemble, one has to replace A_p and Σ_p in Eq. (13) with A_{sh} and Σ_{sh} , respectively. For the compactivity ensemble, we write

$$\frac{P(V, \chi_1)}{P(V, \chi_2)} = \frac{Z_N^{\chi_2}}{Z_N^{\chi_1}} e^{-(\frac{1}{\chi_1} - \frac{1}{\chi_2})V}. \quad (14)$$

IV. DATA

To prepare packings, we use computer simulations in 3D. We generate packings of $N = 10^4$ particles with periodic boundary conditions. In the first stage, we prepare mechanically unstable particle configurations with the Lubachevsky-Stiller algorithm [18,19] with the implementation from Refs. [20–22]. These very systems were presented and studied in Ref. [20]. In the second stage, these particle configurations were stabilized with frictional forces by the protocol and the TRUBAL software package from Refs. [8,23–25]. The TRUBAL algorithm assumes that spheres have small soft shells with a harmonic potential and attempts to find the lowest overlap between spheres to make sure that a packing is mechanically stable. We used friction coefficient $\mu = 10^4$. We produced 293 stable packings in the density range $\varphi = 0.56–0.72$.

V. RESULTS AND DISCUSSION

In this section, we calculate angoricities, keramicities (discussed in detail below), and compactivity and discuss the results. We at first present the steps for calculating pressure angoricity, inspect the pressure angoricity EOS, then briefly present the calculation of the shear angoricity and discuss the shear angoricity EOS. We then investigate keramicities. Finally, we calculate compactivities and analyze compactivity EOS.

A. Calculating angoricity

For equilibrated subsystems, we use in the main text groups of $N_{\text{grp}} = 8$ particles, following Ref. [10] (see Fig. 3 there) and Ref. [11] (see also the review [1]). The rest of the packing will be considered as a “thermal” bath. The value $N_{\text{grp}} = 8$ is not the only one used in the literature: Reference [17] studies finite-size effects and investigates $N_{\text{grp}} = 1–200$ (2D systems, compactivity only). Reference [12] presents an extensive analysis of finite-size effects for 2D disks. In Appendix F, we investigate the effects of the group size on angoricity measurements. We find that the EOS coefficient in the thermodynamic limit differs only marginally from its value for $N_{\text{grp}} = 8$, so we focus on $N_{\text{grp}} = 8$ in the main text.

Prior to splitting packings into groups, calculating force-moment tensors, Voronoi tessellations, and granular temperatures, we remove rattler particles from the packings. Rattler particles are those that do not contribute to the jamming (force-bearing) backbone of a packing, and we mark particles with less than three contacts as rattlers. Removing rattler particles was in our experience a crucial step to produce

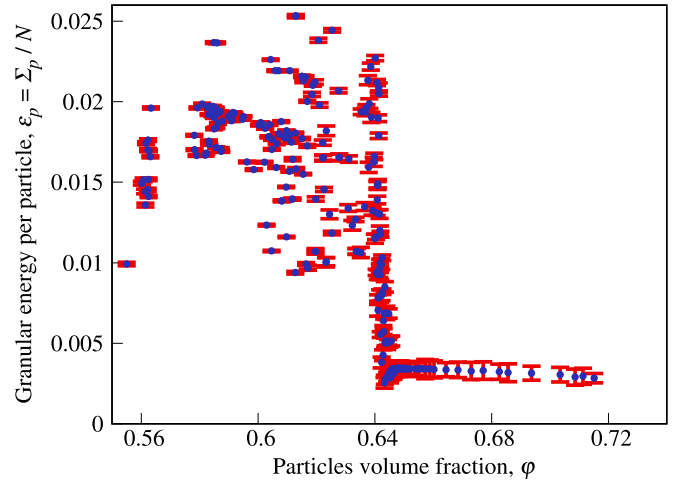


FIG. 1. Granular energies in the pressure angoricity ensemble per particle $\varepsilon_p = \Sigma_p/N$ vs packing density φ . Compression components of the force-moment tensor (granular energies) per particle are relatively high at low densities and exhibit a drop at $\varphi = 0.64–0.65$, around the RCP limit $\varphi = 0.64$. It happens because $\varphi = 0.64$ is the lowest density where mechanically stable frictionless packings can exist (and at $\varphi = 0.65$, crystalline inclusions start to appear). So at $\varphi \geq 0.64$, no friction is needed to keep packings stable, and, hence, no normal forces are needed. It means that the force-moment tensor trace can also rapidly drop at $\varphi = 0.64–0.65$. Error bars indicate 99.7% (3-sigma) confidence intervals, calculated from standard deviation of Σ_p for subpackings of size $N_{\text{grp}} = 8$.

reasonable results. Without removing rattlers, the method of overlapping histograms was not applicable (log differences of granular energy histograms did not typically look linear). We believe it makes physical sense since rattler particles do not contribute to the force-bearing network of particle contacts. Around 2% of particles are rattlers, which means that our packings contain $\sim 9800/8 = 1225$ nonoverlapping groups of $N_{\text{grp}} = 8$ particles.

To determine a new connected group of particles, we select an initial “center” particle (among particles not yet participating in other subsystems), then select a shell of particles that are in contact with the center particle (which, in addition, are nonrattlers and do not belong to other groups), then select particles that are in contact with the first shell, and so on, until we reach N_{grp} particles in this group. We repeat this process of group selection until all nonrattler particles belong to a group (or no groups of N_{grp} particles can be constructed).

Figure 1 presents compression components of the force-moment tensor (granular energies in the pressure angoricity ensemble) per particle Σ_p/N vs packing density φ . To calculate Σ_p , we took entire packings of $N = 10^4$ particles. As explained in the caption, the energies exhibit a rapid drop at $\varphi = 0.64–0.65$ because for $\varphi \geq 0.64$ one can produce mechanically stable frictionless packings, and the force-moment tensor can be zero (given that the TRUBAL algorithm attempts to find the configuration with the smallest forces that still ensure mechanical stability).

The error bars in Fig. 1 indicate 99.7% (3-sigma) confidence intervals, calculated from averaging over subpackings. They are relatively small compared to the actual scatter of

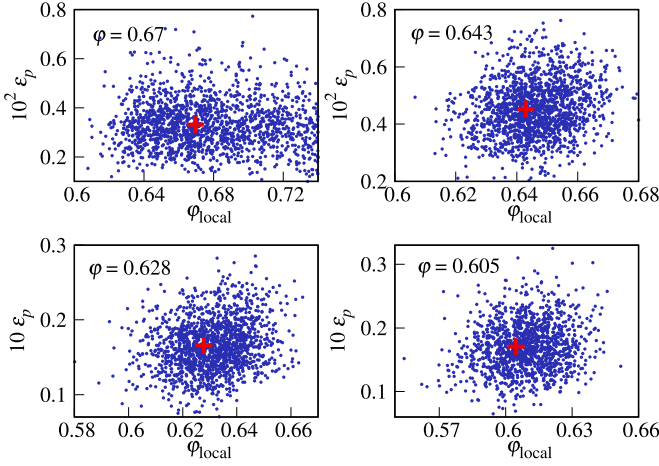


FIG. 2. Local density and local granular energy clouds in the pressure angoricity ensemble. Each point represents a nonoverlapping subpacking of $N_{\text{grp}} = 8$ particles along with its local density φ_{local} and local granular energy per particle $\varepsilon_p = \Sigma_p/N_{\text{grp}}$ in a given subpacking. It is a visualization of joint probability density functions $f(\varphi_{\text{local}}, \varepsilon_p)$. There seems to be no strong dependence of a conditional distribution $f(\varepsilon_p|\varphi_{\text{local}})$ on φ_{local} . Red crosses represent global values of each packing as a whole.

points. The angoricity estimates determined below also have relatively small error bars for a particular packing, but they are also highly scattered between packings. At the same time, the EOS that we determine below looks much less scattered, so angoricities and energies align well. We interpret this situation as follows: variance between subpackings in a given packing is small enough to lead to high confidences in estimates of different measurements, but packing properties are subject to large fluctuations during the process of packing generation. At the same time, angoricity and corresponding granular energy in each packing align well and the final EOS holds well.

Since we treat small subpackings of N_{grp} particles as equilibrated subsystems, each subsystem can have a local density (as computed from Voronoi tessellation) and a local granular energy $\varepsilon_p = \Sigma_p/N_{\text{grp}}$ that are different from average packing values. We visualize their joint probability distributions in Fig. 2. Each panel represents a packing at a given φ , and the red cross represents average values for the entire packing. Each blue dot represents a subpacking with $N_{\text{grp}} = 8$ particles, i.e., each panel contains ~ 1200 points. The plots indicate that there is no strong dependence of a conditional distribution $f(\varepsilon_p|\varphi_{\text{local}}) = f(\varphi_{\text{local}}, \varepsilon_p)/f(\varphi_{\text{local}})$ on φ_{local} , i.e., $f(\varepsilon_p|\varphi_{\text{local}}) \approx f(\varepsilon_p)$ where $f(\varepsilon_p) = \int f(\varphi_{\text{local}}, \varepsilon_p)d\varphi_{\text{local}}$.

Local subpacking volume can impact the distribution $f(\varepsilon_p)$ either as an additional external variable or as an additional energy variable [cf. Eq. (9)]. To exclude potential impact of local packing volume (or density) on angoricity and compactivity calculations, we ideally need to select subpackings in a narrow interval of $\varphi_{\text{local}} \rightarrow \varphi$ (so that local packing density matches global density). To analyze how large the interval of local densities around φ can be, we select in three packings a different number of subpackings with φ_{local} closest to φ and build distributions of $f(\varepsilon_p)$ in Fig. 3. Since Fig. 2 hints that $f(\varepsilon_p|\varphi_{\text{local}}) \approx f(\varepsilon_p)$, we expect that the distribution shall be independent of how many subpackings we take for building

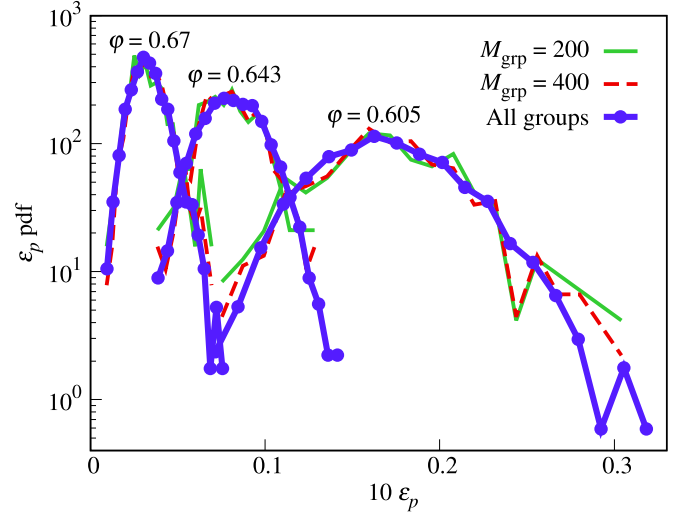


FIG. 3. Probability density functions (PDFs) for local energies $\varepsilon_p = \Sigma_p/N_{\text{grp}}$ of subpackings, depending on how many (M_{grp}) subpackings with suitable φ_{local} (close to packing φ) we select for calculation. Ideally, we need to calculate $f(\varepsilon_p|\varphi)$, i.e., select only a small number of subpackings whose local densities are close to the global packing density, $\varphi_{\text{local}} \approx \varphi$. This makes histograms very noisy and calculations unreliable. Since $f(\varepsilon_p|\varphi_{\text{local}}) \approx f(\varepsilon_p)$ (cf. also Fig. 2), we calculate the PDFs by taking more and more subpackings with densities φ_{local} closest to φ . The plots demonstrate that it is safe to take all the subpackings ($M_{\text{grp}} \approx 1200$) in a given packing (i.e., $f(\varepsilon_p)$) to estimate $f(\varepsilon_p|\varphi)$, which is consistent with Fig. 2.

a histogram, and we can use the entire packing. Figure 3 confirms this assumption. Hence, in the remainder of this work, to obtain better statistics for the overlapping histograms method, we use all the subpackings for building histograms. Conversion between distributions per particle $f(\varepsilon_p)$ and per subpacking $P(\Sigma_p)$ from Eq. (12) is explained in Appendix A.

Figure 4 depicts the log-ratios of $f_1(\varepsilon_p)/f_2(\varepsilon_p)$ along with their linear fits. The fits are performed over bins where the number of subpackings is > 10 (for both histograms). The red dashed lines in Fig. 4 stop at the edges where at least one of the two overlapping histogram bins has < 10 subpackings. Excluding histogram bins with insufficient number of subpackings is essential to obtain proper estimates of inverse granular temperatures further in the paper and to produce low confidence intervals for these estimates. Figure 4 demonstrates that the assumptions of the overlapping histograms method [Eq. (13)] are justified. Appendix B and Fig. 9 there present details on goodness of linear fits in the overlapping histograms method. They show that the applicability of linear fits deteriorates at $\varphi \sim 0.65$, which is expected because monodisperse packings contain crystalline inclusions at $\varphi > 0.65$, and the assumptions of statistical mechanics do not completely apply in this density range (specifically, the assumption of equiprobable microstates). We found though that including points with $\varphi > 0.65$ does not change the final EOS for pressure angoricity but improves confidence intervals, so we will estimate the final EOS for pressure angoricity with all densities [for more details, cf. Fig. 13(d) in Appendix E].

After calculating the differences of inverse pressure angoricities between all the packings according to Eq. (13) we

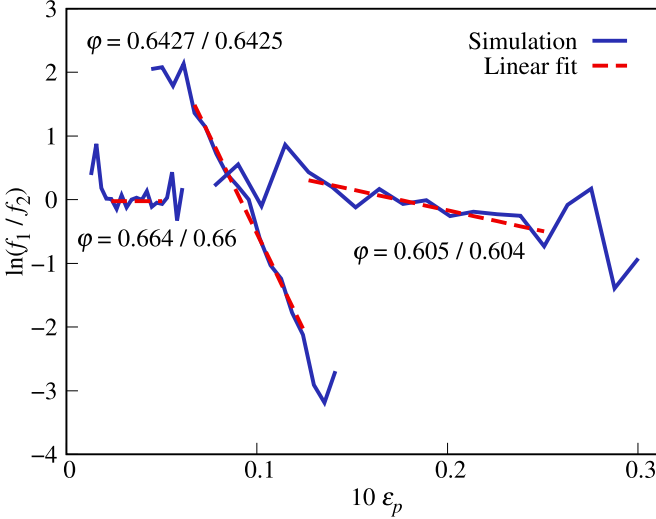


FIG. 4. Log energy differences for the overlapping histograms method [Eq. (13)] in the pressure angoricity ensemble. Here we display the ratio of logarithms of probability density functions for energies per particle from Fig. 3, $f_1(\varepsilon_p)/f_2(\varepsilon_p)$, along with their fits. We omit from the fitting procedure bins with < 10 subpackings, and the red dashed lines stop at the edges where at least one of the two overlapping histograms has < 10 subpackings in a bin. The differences of logarithms look like straight lines indeed, so the method of overlapping histograms is applicable.

estimate inverse pressure angoricities up to an unknown constant $\frac{1}{A_p} - C_{A,p}$. The plot of $\frac{1}{A_p} - C_{A,p}$ vs φ can be found in Fig. 5. In more detail, for each packing, we determine histogram differences with 10 other packings of higher densities and take the average value of $\frac{1}{A_p} - C_{A,p}$. We start from the highest packing density and in an iterative manner determine $\frac{1}{A_p} - C_{A,p}$ for all the packings going to lower densities. We

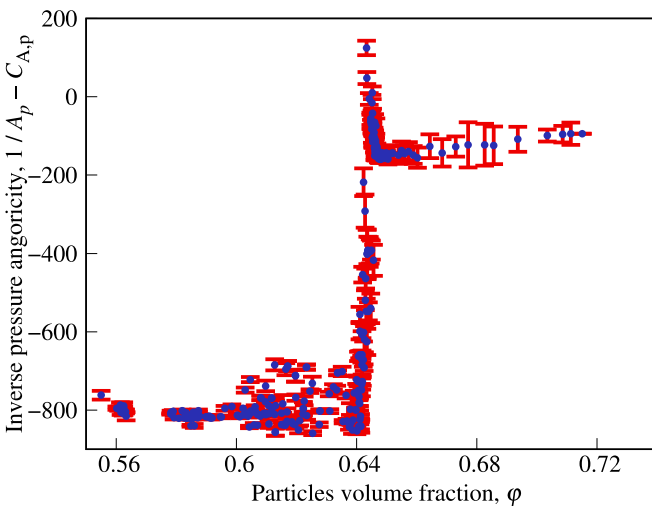


FIG. 5. Inverse pressure angoricities up to an unknown constant $\frac{1}{A_p} - C_{A,p}$ vs packing density φ . Error bars represent 3-sigma (99.7%) confidence intervals, where standard deviations are taken from 10 estimates of inverse pressure angoricities from histogram overlaps with 10 packings of higher densities.

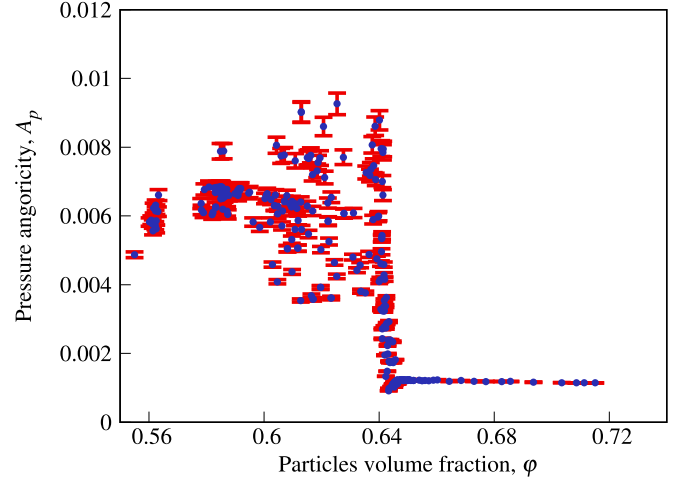


FIG. 6. Pressure angoricities A_p vs packing densities φ . Pressure angoricities exhibit a drop at $\varphi \approx 0.64$ – 0.65 , similarly to granular energies Σ_p in Fig. 1. Error bars correspond to 95% confidence intervals estimated from the delta method, where we incorporate uncertainty in fits as well as uncertainties from the estimates from Fig. 5.

perform the final step for calculating angoricities A_p (fitting $C_{A,p}$ and EOS) in the next subsection.

B. Pressure angoricity EOS

Following Refs. [1,7,10], we aim to fit the granular EOS for pressure angoricities with

$$\langle \Sigma_p \rangle = N_{\text{grp}} k_{A,p} A_p, \text{ or } \langle \varepsilon_p \rangle = k_{A,p} A_p, \quad (15)$$

where averaging is over subpackings. If we denote $\frac{1}{A_p} - C_{A,p}$ determined up until now as x , then we in fact fit the nonlinear relation,

$$\langle \varepsilon_p \rangle = k_{A,p} \frac{1}{x + C_{A,p}}, \quad (16)$$

with two unknowns $k_{A,p}$ and $C_{A,p}$. For ε_p , one can either take $\langle \varepsilon_p \rangle$ (average of energies per particle over subpackings) or the values from Fig. 1, i.e., granular energies of entire packings divided by the total number of particles.

The values of A_p vs φ are depicted in Fig. 6. The values of $\varepsilon_p = \Sigma_p/N_{\text{grp}}$ vs A_p along with the linear fit are depicted in Fig. 7(a), where $k_{A,p} = 2.81 \pm 0.08$ (95% confidence intervals, the calculation includes uncertainties from Fig. 5). For completeness, $C_{A,p} = 969 \pm 4$. Figure 7(a) also depicts the values for shear components of the force-moment tensor $\Sigma_{\text{sh}}/N_{\text{grp}}$ vs shear angoricities A_{sh} , which we discuss in the next subsection.

Figure 7(a) demonstrates that the EOS Eq. (15) works very well for granular systems under study. The R^2 value of the fit for pressure angoricity is 0.995. Figure 9 in Appendix B provides more details on the goodness of fit of overlapping histograms.

Reference [7] introduces a version of the EOS that includes the average coordination number z [Eq. (17) there]. To check the influence of z of a subpacking on the pressure angoricity EOS, we include z into the EOS and fit the

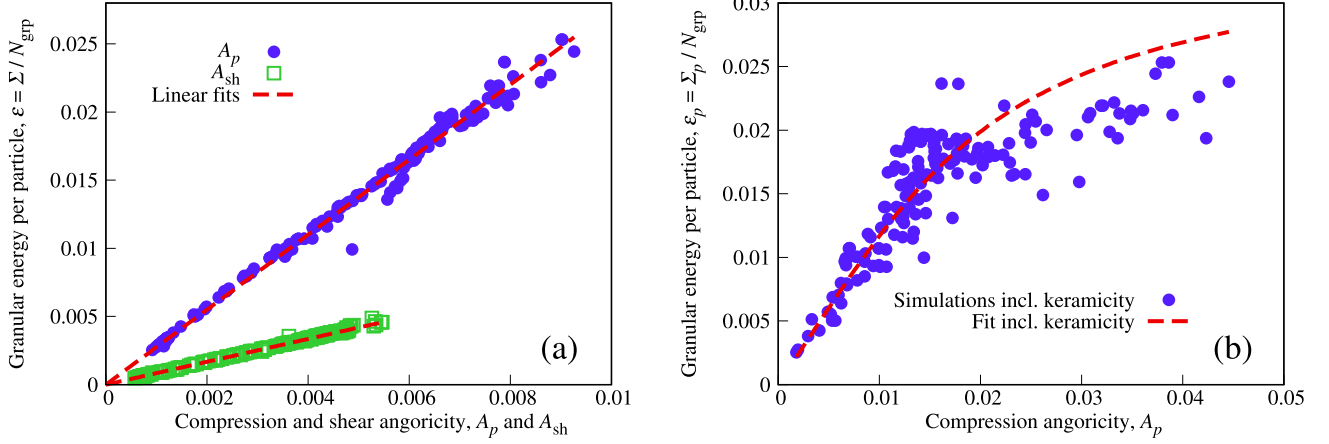


FIG. 7. Granular energy (pressure and shear components of the force-moment tensor) vs different versions of granular temperature (pressure angoricity, shear angoricity, and inverse ceramicity). (a) Pressure components of the force-moment tensor per particle $\langle \varepsilon_p \rangle = \langle \Sigma_p \rangle / N_{\text{grp}}$ vs angoricities A_p and shear components of the force-moment tensor $\langle \Sigma_{\text{sh}} \rangle / N_{\text{grp}}$ vs shear angoricities A_{sh} along with respective linear fits $\langle \Sigma_p \rangle = N_{\text{grp}} k_{A,p} A_p$ and $\langle \Sigma_{\text{sh}} \rangle = N_{\text{grp}} k_{A,\text{sh}} A_{\text{sh}}$. Here $k_{A,p} = 2.81 \pm 0.08$ and $k_{A,\text{sh}} = 0.85 \pm 0.01$ (95% confidence intervals). (b) Pressure components of the force-moment tensor per particle $\langle \varepsilon_p \rangle = \langle \Sigma_p \rangle / N_{\text{grp}}$ vs angoricities A_p when determined from full fits [Eq. (20)] to histogram log-differences, which also account for ceramicities κ . The red line is from the EOS fit in the form of Eq. (22), which can be interpreted as dependence $\langle \varepsilon_p \rangle = f(A_p, \kappa^{-1})$. The full depiction of the data from simulations and the EOS fit in 3D can be found in Fig. 13(c) in Appendix E. The present panel is the projection of the 3D data onto the plane $A_p, \langle \varepsilon_p \rangle$.

latter in the form $\langle \Sigma_p \rangle / N_{\text{grp}} = k_{A,p} A_p + a_z(z - z_0) + b_z(z - z_0)^2$, which actually means that we perform a nonlinear fit $\langle \Sigma_p \rangle / N_{\text{grp}} = k_{A,p} \frac{1}{x + C_{A,p}} + a_z(z - z_0) + b_z(z - z_0)^2$. The resulting fit reads $\langle \Sigma_p \rangle / N_{\text{grp}} = 2.73 A_p + 0.00166(z - 4.52) + 0.00096(z - 4.52)^2$ with goodness of fit $R^2 = 0.996$. Given that the goodness of fit barely changes, we conclude that it is not necessary to include the average coordination number of a subpacking into the EOS. If we use the more formal Akaike information criterion or the Bayesian information criterion to compare the two models, we reach the same conclusion.

The form of Eq. (15) is predicted for frictionless particles by the mean-field theory [1,7]. Our packings are frictional, and applicability of the theory is not granted. The mean-field theory (Eq. (23) in Ref. [7]) predicts at the isostatic point

$$\langle \Sigma_p \rangle = \frac{z_{\text{iso}}}{2} N_{\text{grp}} A_p, \quad (17)$$

where z_{iso} is the isostatic contact number, which for 3D systems is 6. The original paper uses Γ and α , $\alpha = \frac{N_{\text{grp}} z_{\text{iso}}}{2\Gamma}$, and in our notation $A = 1/\alpha$ and $\Gamma/A = \Sigma_p/A_p$, so the same proportionality constant remains. Our simulation result is very close to the theoretical prediction of $k_{A,p} = 3$. Interestingly, Ref. [10] reports for 2D frictional packings that the form of the equation holds but the proportionality coefficient in their simulations differs stronger than in our case ($1/0.153 = 6.53$ from simulations vs 2 from theory).

C. Shear angoricity EOS

To calculate shear angoricities [cf. Eq. (10)] and their EOS, we repeat the steps for pressure angoricities and present them in Appendix C and Fig. 10 there. The data for shear angoricities looks quantitatively similar to the data for pressure angoricities.

Figure 7(a) presents final results for shear angoricity calculations, i.e., shear components of the force-moment tensor $\Sigma_{\text{sh}}/N_{\text{grp}}$ from Eq. (10) vs corresponding shear angoricities A_{sh} .

One difference between shear and pressure angoricities is that we found it impossible to include points with $\varphi > 0.67$ to estimate the EOS for shear angoricities, so we only include points with $\varphi \leq 0.67$ into Fig. 7(a) for A_{sh} . We speculate that it is because packings are not completely random at high densities (it is known that crystalline inclusions start appearing at $\varphi > 0.65$ [26]), the underlying assumptions of the statistical theory do not apply completely (like the assumption of equiprobable microstates), and the overlapping histogram methods also does not apply fully, hence goodness of linear fits deteriorates too much. Goodness of fit is presented in Figs. 10(e) and 10(f) in Appendix C, and the drop at $\varphi = 0.65$ is pronounced there. A similar drop in the goodness of linear fits for A_p is visible in Fig. 9 in Appendix B, but it turned out that our estimates for A_p EOS where consistent for density ranges $\varphi \leq 0.65$, $\varphi \leq 0.67$, and $\varphi < \infty$, and, hence, for A_p , we used and presented in Fig. 7(a) all available data points [cf. also Fig. 13(d) in Appendix E].

Figure 7(a) demonstrates that shear angoricity and shear granular energy follow a linear EOS $\langle \Sigma_{\text{sh}} \rangle = N_{\text{grp}} k_{A,\text{sh}} A_{\text{sh}}$ very well, with coefficient of determination $R^2 = 0.998$. The slope of the fit is $k_{A,\text{sh}} = 0.85 \pm 0.01$ and the constant $C_{A,\text{sh}}$, equivalent to $C_{A,p}$ for pressure angoricities, is $C_{A,\text{sh}} = 998 \pm 4$.

Interestingly, the ratio between slopes for both angoricities in our measurements ($2.8/0.85 = 3.29$) is similar to the ratio between equivalent slopes for 2D frictional packings from Ref. [10]. Reference [10] presents angoricity vs granular energy, so we invert their slopes, which gives $0.450/0.153 = 2.94$.

We confirm that the results for the shear angoricity calculated from Eq. (11) (the root mean square of the shear

component of the force-moment tensor) are quantitatively very similar and proportionality constant in the EOS is $k_{A,\text{sh}} = 0.83 \pm 0.01$.

We believe that the results for shear angoricity in 3D are less trivial than for the pressure angoricity. Specifically, if we assume that every element of the force-moment tensor $\hat{\Sigma}_{ij}$ has a Boltzmann distribution, then its compression component $\text{Tr}\hat{\Sigma} = (\hat{\Sigma}_{11} + \hat{\Sigma}_{22} + \hat{\Sigma}_{33})/3 = (\Sigma_1 + \Sigma_2 + \Sigma_3)/3$ is expected to have at least the Gamma distribution (and in fact seems to be exponential—which may follow from the systems being isotropic). But the maximum shear component $(\Sigma_1 - \Sigma_3)/2$ is not a tensor invariant, and its calculation from an arbitrary frame of reference involves nonlinear operations (finding principal axes and eigenvalues). Finding the RMS shear from Eq. (11) involves even more nonlinear calculations. In our view, it is nontrivial that the shear component of the force-moment tensor obeys the same statistical mechanics (has the Boltzmann distribution) as the compressional component. We are not aware of theoretical works that explain this empirical observation, and it requires further analysis and explanation.

D. Higher-order terms in log-differences: Estimating keramicity

Recent results [11–13] suggest that there is another extensive quantity in granular systems, which for 2D systems is the so-called Maxwell-Cremona force-tile area $b = \det\hat{\Sigma}/V$, where V is system volume [cf. Eq. (34) in Ref. [12], where it is denoted as A_R]. It was introduced in Refs. [27,28]. For 2D isotropic systems, given that $\hat{\Sigma}_{i,j} = \Sigma_p \delta_{i,j}$ (where $\delta_{i,j}$ is the Kronecker delta), $b = \Sigma_p^2/V$. For 3D isotropic systems, $b = \Sigma_p^3/V$. Theoretical work in the mean-field limit [13] derives such an equivalent additive quantity, $b = \int dV \det\hat{\Sigma}/V$ (cf. Eq. (13) in Ref. [13]). It indeed seems to be a good candidate for granular energy since determinant is one more tensor invariant with respect to rotations, along with trace. The authors of Ref. [13] call such quantity for 3D systems the Beltrami volume, we will adopt this term below as well. For discrete particle systems, this quantity simply extends to $\det\hat{\Sigma}$. The authors of Ref. [11] call the corresponding reciprocal temperature-like variable “keramicity” κ (denoted as λ in Ref. [12]). Keramicity is an inverse temperature variable, similarly to α from Eq. (6).

After introducing keramicity and the corresponding reciprocal extensive energy variable $\det\hat{\Sigma}$ for granular systems, the exponent in Eq. (12) becomes

$$\exp\left(-\frac{\Sigma_p}{A_p} - \kappa \det\hat{\Sigma}\right) \quad (18)$$

and histogram differences shall be fitted with a plane. As discussed in Refs. [11,12,28,29], under the assumption that $\det\hat{\Sigma}$ is strongly peaked around Σ_p^3 (for 2D systems, around Σ_p^2), one can replace $\det\hat{\Sigma}$ in this exponent with Σ_p^3 . For generality, we assume $\det\hat{\Sigma} = a\Sigma_p^3$. The exponent then becomes

$$\exp\left(-\frac{\Sigma_p}{A_p} - \kappa a \Sigma_p^3\right), \quad (19)$$

Eq. (12) in Ref. [12] includes a finite-size scaling factor for κ , subsystem volume V , which is proportional to the number

of particles in the group. We perform investigations with a fixed $N_{\text{grp}} = 8$, so we omit this factor for simplicity, following Ref. [11]. When fitting log-differences of histograms, one obtains as fitted parameters differences in both quantities, $\Delta\alpha_p = \frac{1}{A_{p1}} - \frac{1}{A_{p2}}$ [cf. Eq. (13)] and $\Delta\kappa$:

$$\frac{\ln P_1}{\ln P_2} = B + \Delta\alpha_p \Sigma_p + \Delta\kappa a \Sigma_p^3. \quad (20)$$

Similarly to $\frac{1}{A_p}$, we accumulate κ (by using log-differences with previous 10 packings) and get the estimates up to an unknown constant C_κ .

Appendix E presents details on using higher-order fits. Figure 12 there demonstrates that even for subpackings of $N_{\text{grp}} = 8$ the relation $\det\hat{\Sigma} = a\Sigma_p^3$ applies. For packings in the range of densities $\varphi = 0.58\text{--}0.65$, $a \approx 0.91$, so we can utilize Eq. (19) for packings in this density range.

Figure 13 in Appendix E presents the details of fits with Eqs. (19) and (20). Figure 13(a) demonstrates that inverse angoricities remain quantitatively similar to the results from linear fits. Figure 13(f) demonstrates that inverse keramicities, if estimated from Eq. (19), strongly deviate from expected behavior for $\varphi > 0.644$. For the range $\varphi > 0.65$, one reason is that replacing $\det\hat{\Sigma}$ with $a\Sigma_p^3$ is not valid, presumably because packings become partially crystallized, so the full fit with Eq. (18) shall be used. Thus, for studying keramicities, we only take packings in the range $\varphi = 0.58\text{--}0.644$.

Reference [13] provides a theoretical framework for constructing a combined EOS $\langle \Sigma_p \rangle = N_{\text{grp}} f(A_p, \kappa^{-1})$. Specifically, for repulsive isotropic 2D materials, they derive, in our notation, $\alpha_p \langle \varepsilon_p \rangle + \kappa \langle \varepsilon_p \rangle^2 = \text{const}$ [cf. Section IV B there, as well as Eq. (64) there]. Equation (64) in Ref. [13] includes one more parameter, η , but the authors argue in Sec. IV A of that paper that this parameter and the corresponding term can be neglected for systems with purely repulsive potential near the jamming point. Hence, we also neglect this parameter in the present paper. Extension of this EOS to 3D systems leads to

$$\alpha_p \langle \varepsilon_p \rangle + \kappa \langle \varepsilon_p \rangle^3 = \text{const}. \quad (21)$$

A simpler approach from Ref. [11] is to fit a separate EOS for $\langle \Sigma_p \rangle$ vs $N_{\text{grp}} \kappa^{-1}$. The authors of Ref. [12] were able to fit the EOS for 2D systems in the form $\langle \Sigma_p \rangle \sim N_{\text{grp}} \kappa^{-1/2}$. When using such a simplified approach, we could not fit keramicity either with a linear EOS $\langle \Sigma_p \rangle \sim N_{\text{grp}} \kappa^{-1}$ or with a cubic EOS $\langle \Sigma_p \rangle \sim N_{\text{grp}} \kappa^{-1/3}$. We could describe the data with a form $\langle \Sigma_p \rangle \sim N_{\text{grp}} \kappa^{-1/2}$ well, but it is nonphysical since it implies that the proportionality constant in 3D is dimensional. At the same time, our data comply well with the theoretically predicted form (21) of the EOS. Given that theoretical results are derived in the mean-field limit, we allow some freedom in proportionality constants and fit the EOS with keramicity in the form $\alpha_p \langle \varepsilon_p \rangle + D\kappa \langle \varepsilon_p \rangle^3 = C$ or

$$\frac{1}{A_p} \langle \varepsilon_p \rangle + D\kappa \langle \varepsilon_p \rangle^3 = C. \quad (22)$$

Similarly to Eq. (16), it is a more complex fit. If we denote with x and y inverse angoricity and keramicity values determined from simulations up to constants $C_{A,p}$ and C_κ , respectively, then the full fit is $(x + C_{A,p}) \langle \varepsilon_p \rangle + D(y + C_\kappa) \langle \varepsilon_p \rangle^3 = C$.

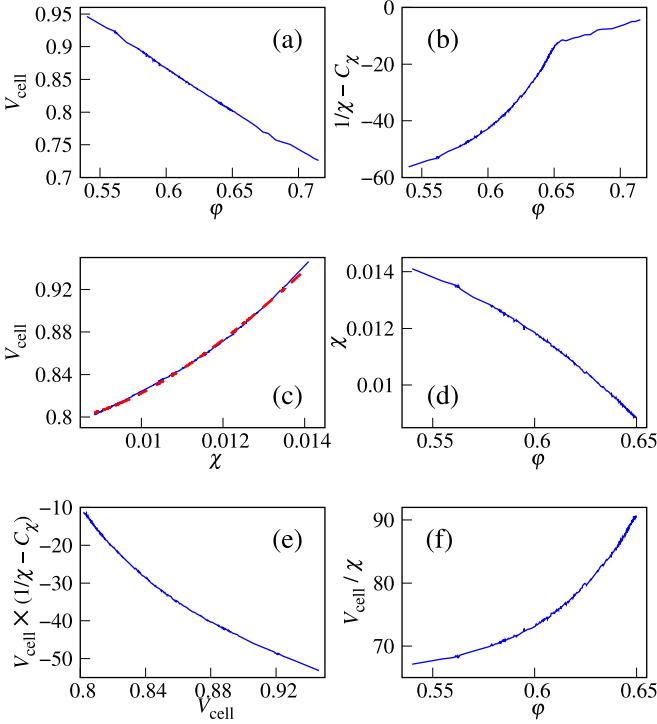


FIG. 8. Compactivity χ fits. (a) Average volume of Voronoi cells, $V_{\text{cell}} = \langle V_{\text{grp}} \rangle / N_{\text{grp}}$, where V_{grp} is the volume of a subpacking of $N_{\text{grp}} = 8$ particles. Apart from a small noise due to averaging, it follows an analytical curve $V_{\text{cell}} = \frac{\pi}{6} D^3 \frac{1}{\varphi}$, where the sphere diameter $D = 1$. (b) Inverse compactivity $1/\chi$ up to an unknown constant C_χ determined by the method of overlapping histograms. (c) EOS V_{cell} vs χ after fitting it with the form $V_{\text{cell}} = a\chi + b/\chi$ (the unknown constant C_χ is fitted implicitly). The red dashed line is the fit. The fit was performed for $\varphi \leq 0.65$. (d) χ vs φ . Compare with Fig. 4 from Ref. [17] for 2D. (e) $V_{\text{cell}} \times (1/\chi - C_\chi)$ vs V_{cell} . If the EOS had the form $V_{\text{cell}} = a\chi$, this plot would be linear, $a - V_{\text{cell}}C_\chi$. It is not, which means that the EOS is nonlinear. (f) V_{cell}/χ vs φ . If the EOS had the form $V_{\text{cell}} = a\chi$, this plot would be a constant, but it is not. Compare with Fig. 2(c) from Ref. [10].

Numerical fit of EOS (22) to our data in the range $\varphi = 0.58\text{--}0.644$ produces $\frac{1}{A_p} \langle \varepsilon_p \rangle + 0.11\kappa \langle \varepsilon_p \rangle^3 = 1.2$ with parameters $D = 0.11 \in [0.03, 0.21]$ and $C = 1.2 \in [1.15, 1.32]$ (95% confidence intervals). We display the 3D version of the fit in Fig. 13(c) in Appendix E. Blue dots there depict triples $(A_p, \kappa^{-1}, \langle \varepsilon_p \rangle)$ determined from simulations for each granular packing. The surface represents the EOS fit (22), which can be interpreted as a 3D plot $\langle \varepsilon_p \rangle = f(A_p, \kappa^{-1})$. Figure 7(b) presents a projection of this 3D plot onto axes A_p and $\langle \varepsilon_p \rangle$, since A_p has a much stronger influence on $\langle \varepsilon_p \rangle$. These plots demonstrate that the theoretically predicted EOS (22) is able to describe our data well. The differences with the works of Refs. [11,12], i.e., inability to fit the data with a simple EOS independent of A_p , can be the target of future studies.

E. Compactivity EOS

Figure 8 presents results of the compactivity analysis through the method of overlapping histograms, similarly to the angoricity and keramicity results above.

Figure 8(a) depicts average Voronoi cell volumes (granular energies) computed as $\langle V_{\text{cell}} \rangle = \langle V_{\text{grp}} \rangle / N_{\text{grp}}$, where V_{grp} is

the volume of a subpacking of $N_{\text{grp}} = 8$ particles. It follows an analytical curve $V_{\text{cell}} = \frac{\pi}{6} D^3 \frac{1}{\varphi}$ (with the sphere diameter $D = 1$), apart from small noise due to averaging.

Figure 11 in Appendix D presents additional related panels: Figure 11(a) provides probability density functions of Voronoi volumes of subpackings V_{grp} and is equivalent to Fig. 3. Figure 11(b) demonstrates differences between probability density functions of Voronoi volumes of subpackings in the log scale and is equivalent to Fig. 4 for pressure angoricity. Figures 11(c) and 11(d) present goodness of linear fits for the method of overlapping histograms.

Figure 8(b) is equivalent to Fig. 5 and presents inverse compactivities $1/\chi$ up to an unknown constant C_χ as determined from the method of overlapping histograms. There is a kink at $\varphi \approx 0.65$, where packings start obtaining crystalline structure (cf. Ref. [26]). At this density, the assumptions of the method of overlapping histograms break since the logarithms of overlapping histograms stop following linear fits [as depicted in Figs. 11(c) and 11(d) in Appendix D].

Figure 8(c) represents the final compactivity EOS ($V_{\text{cell}} = \langle V_{\text{grp}} \rangle / N_{\text{grp}}$) vs χ and the fit (red dashed line) in the form

$$\langle V_{\text{cell}} \rangle = \frac{\langle V_{\text{grp}} \rangle}{N_{\text{grp}}} = a\chi + \frac{b}{\chi}. \quad (23)$$

We implicitly determined the unknown constant C_χ with this fit. More precisely, if we denote with x the value $1/\chi - C_\chi$ determined from the overlapping histograms method, then the final fit looked like $V_{\text{cell}} = \frac{a}{x+C_\chi} + b(x+C_\chi)$. The form of Eq. (23) is unnatural for an EOS since it implies that granular energy V_{cell} diverges at zero granular temperature. Divergence of V_{cell} is not physical, and we interpret it as being impossible for χ to reach zero. We could not find a better fitting form, and the fact that this is the only simple EOS form that fits our compactivity data is one of the reasons we believe compactivity is a less suitable temperature-like variable for granular matter. We note that we could only fit the range of $\varphi \leq 0.65$ for compactivity EOS, contrary to pressure angoricity fits (see the kinks in Fig. 8 at $\varphi \approx 0.65$). Reference [10] [Fig. 2(c) there] presents similar data for 2D frictional disks.

Figure 8(e) demonstrates that the function $V_{\text{cell}}(\chi)$ is nonlinear, even prior to explicit fits. We present the values of $V_{\text{cell}} \times (1/\chi - C_\chi)$ vs V_{cell} . If the EOS $V_{\text{cell}}(\chi)$ had the form $V_{\text{cell}} = a\chi$, then this plot would be linear, $a - V_{\text{cell}}C_\chi$. It is not, which means that the EOS is nonlinear.

Figure 8(f) presents the plot V_{cell}/χ vs φ . Similarly, if the EOS $V_{\text{cell}}(\chi)$ had the form $V_{\text{cell}} = a\chi$, then this plot would be a constant, but it is not. The same approach is used in Ref. [10], Fig. 2(c) there. The authors of Ref. [10] shifted χ so that it is ∞ at the RLP limit. We take the values of χ (i.e., the constant C_χ) as determined by the fit in Fig. 8(c), Eq. (23).

VI. SUMMARY AND CONCLUSIONS

In this work, we investigated statistical mechanics of granular media for three-dimensional frictional monodisperse hard spheres. We measured pressure and shear angoricities, as well as keramicity and compactivity for systems under study. To the best of our knowledge, this is the first time when pressure

angoricitities, shear angoricitities, and keramicities are estimated for frictional three-dimensional spheres.

As Fig. 7(a) demonstrates, pressure angoricity and the compression component of the force-moment tensor, as well as shear angoricity and shear component of the force-moment tensor, follow a simple and theoretically supported EOS Eq. (15), $\langle \Sigma_p \rangle = 2.8N_{\text{grp}}A_p$ for pressure angoricity and $\langle \Sigma_{\text{sh}} \rangle = 0.85N_{\text{grp}}A_{\text{sh}}$ for shear angoricity. It shows that angoricities and force-moment tensor components can play a role of granular temperature and granular energy, respectively. The recovered EOS is in close correspondence to the theoretical predictions from the mean-field theory for frictionless particles [1,7], which for pressure angoricity in 3D predicts $\langle \Sigma_p \rangle = 3N_{\text{grp}}A_p$. We note that simulations for 2D frictional spheres [10] uncovered a similar linear EOS but with a coefficient that differs from the theoretical predictions stronger.

Figure 7(b) presents a projection of the EOS when another inverse temperature-like variable is introduced, keramicity κ [11,12]. Keramicity is reciprocal to the determinant of the force-moment tensor. When determinant values are distributed narrowly around Σ_p^3 , one can fit histogram log-differences as 1D curves against Σ_p with Eq. (20) and determine both keramicities and pressure angoricities. Keramicity corresponds to the third term in log-differences of granular energy histograms, while angoricity corresponds to the linear term. Theoretical mean-field considerations [13] predict a combined EOS for both keramicities and pressure angoricities in the form of Eq. (21). We could fit our data well with a slightly more generic form (22). Equation (22) essentially defines a surface $\langle \Sigma_p \rangle / N_{\text{grp}} = f(A_p, \kappa^{-1})$. We present the 3D surface and corresponding data points $(A_p, \kappa^{-1}, \langle \Sigma_p \rangle / N_{\text{grp}})$ in Fig. 13(c) in Appendix E and present its projection onto the variables $(A_p, \langle \Sigma_p \rangle / N_{\text{grp}})$ in Fig. 7(b), given that A_p influences $\langle \Sigma_p \rangle$ much stronger. Both figures demonstrate that inverse keramicity and pressure angoricity can serve as state variables for granular systems and conform to the theoretically predicted EOS.

Compactivity χ , on the other hand, seems to follow a more complicated and controversial EOS Eq. (23), which implies that V_{cell} diverges at $\chi = 0$. Divergence of V_{cell} is not physical, and we interpret it as being impossible for compactivity to reach zero values. We conclude that angoricity is therefore a better candidate for granular temperature than compactivity.

As Fig. 6 demonstrates, pressure angoricity experiences a drop at $\varphi = 0.64$ – 0.65 and remains ≈ 0 for higher densities. The same behavior occurs for shear angoricity and keramicity. It happens because frictionless monodisperse packings can be produced for $\varphi \geq 0.64$ [20,30–33], with crystalline inclusions appearing at $\varphi = 0.65$ [34–38]. Our previous results suggest that if crystallization were suppressed, $\varphi = 0.65$ would in fact be the maximum attainable density for monodisperse packings (the glass close packing limit) [20,39,40]. It means that tangential forces are almost not required to keep a packing at $\varphi > 0.64$ stable, and hence normal forces can be negligible, which is why the average value of the compression component of the force-moment tensor Σ_p drops at $\varphi = 0.64$ – 0.65 in Fig. 1 and the distribution of local values of Σ_p shifts to the left and becomes narrower (cf. Fig. 3). The drop in granular energies (Σ_p) can be almost considered trivial from this perspective. If one considers the EOS (7), the drop in pressure

and shear angoricities is also natural, but to the best of our knowledge this form of EOS is only proved for frictionless particles. The drop in angoricity for frictional particles has yet to be proved from first principles. Our results thus provide a distinct view on the “random-close packing” limit $\varphi = 0.64$ – 0.65 as the density interval where granular systems “freeze,” i.e., angoricity (granular temperature) exhibits a drop to a near-zero value.

The data that support the findings of this study are available from the corresponding author upon request.

ACKNOWLEDGMENT

We are very thankful to Professor Karen Daniels for reading the manuscript and providing many insightful comments and suggestions.

APPENDIX A: CONVERTING VALUES PER PARTICLE INTO VALUES PER SUBPACKING

To make Figs. 1–3 comparable, we depicted values per particle. To convert the distributions of energies per particle $f(\varepsilon_p)$ into the distributions of total energies of subpackings from Eq. (12), we use a standard method for changing a variable in probability distributions, $P(\Sigma_p)d\Sigma_p = f(\varepsilon_p)d\varepsilon_p$. Since $\varepsilon_p = \Sigma_p/N_{\text{grp}}$, then $P(\Sigma_p) = f(\Sigma_p/N_{\text{grp}})/N_{\text{grp}}$.

To convert the ratios of f_1/f_2 from Fig. 4 and fit parameters to inverse angoricity differences from Eq. (13), we write $\ln(P_1/P_2) = A + (\frac{1}{A_{p2}} - \frac{1}{A_{p1}})\Sigma_p$ and $\ln(f_1/f_2) = A + (\frac{1}{A_{p2}} - \frac{1}{A_{p1}})N_{\text{grp}}\varepsilon_p$. If we fit $\ln(f_1/f_2)$ with $a + k\varepsilon_p$, then $\frac{1}{A_{p2}} - \frac{1}{A_{p1}} = \frac{k}{N_{\text{grp}}}$.

When fitting log-differences for determining keramicities with the form $\ln(f_1/f_2) = k_0 + k_1\varepsilon_p + k_3\varepsilon_p^3$, which shall correspond to Eq. (20), the following conversion applies: $\ln(P_1/P_2) = \ln(f_1/f_2) = k_0 + k_1\varepsilon_p + k_3\varepsilon_p^3 =$

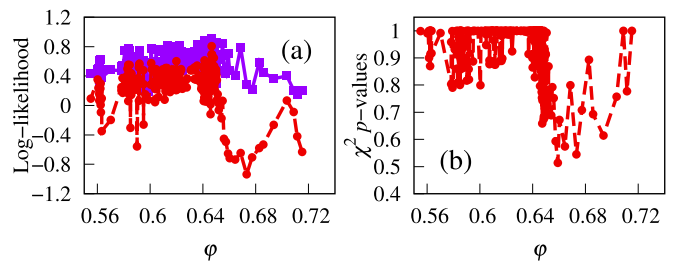


FIG. 9. Goodness-of-fit data for log-differences linear fits for compression angoricity (cf. Fig. 4). (a) Log-likelihoods of fits to log energy differences, Eq. (B1). Red dashed line depicts goodness of fit for linear fits and the purple solid line is constructed for third-order polynomial fits to log-differences. The panel shows that third-order polynomials are sufficient at $\varphi > 0.65$ and for $\varphi \leq 0.65$ linear fits are as good as third-order fits. At the same time, for pressure angoricity, points at $\varphi > 0.65$ comply with the same EOS as points $\varphi \leq 0.65$, so we include them in the final plot Fig. 7(a) for A_p . (b) p values for χ^2 statistics calculated for linear fits as a measure of quality of these fits. The panel shows that for none of the densities we can for sure reject the hypothesis that a fit is linear (p values are never below 0.05) but confirms that fit quality deteriorates for $\varphi > 0.65$.

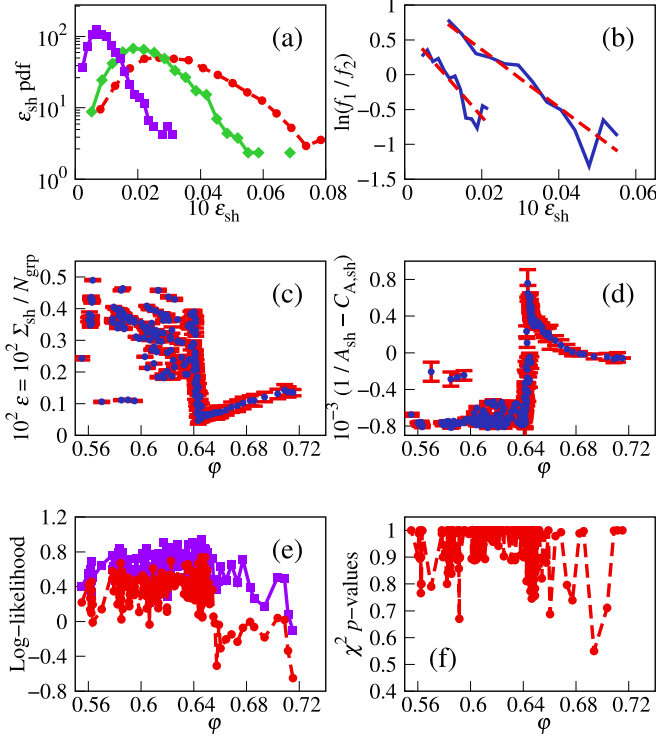


FIG. 10. Details of shear angoricity calculation. Panels (a)–(d) are equivalent to Figs. 1, 3–5, respectively. Panels (e) and (f) are equivalent to Figs. 9(a) and 9(b). (a) Probability distributions of shear components of the force-moment tensor per particle $\epsilon_{sh} = \Sigma_{sh}/N_{grp}$. Histograms are calculated for $M_{grp} \sim 1200$ subpackings (i.e., over $M_{grp} \sim 1200$ values of ϵ_{sh}). Red dashed line (circles): $\phi = 0.605$; green solid line (diamonds): $\phi = 0.641$; and purple solid line (squares): $\phi = 0.669$. (b) Log energy differences for compactivity calculations from the overlapping histograms method, Eq. (14). Similarly to the main text, we display here the ratio of logarithms of probability density functions for energies per particle, $f_1(\epsilon_{sh})/f_2(\epsilon_{sh})$, along with their linear fits. Left blue line: $\phi = 0.6430/0.6431$. Right blue line: $\phi = 0.6047/0.6082$. (c) Granular energies per particle Σ_{sh}/N_{grp} vs packing density ϕ . Error bars have the same meaning as in Fig. 1 (3-sigma confidence intervals). The plot looks qualitatively similar to Fig. 1. (d) Inverse shear angoricities up to an unknown constant $\frac{1}{A_{sh}} - C_{A,sh}$ vs packing density ϕ . Error bars represent 3-sigma (99.7%) confidence intervals, as in Fig. 5. The plot looks qualitatively similar to Fig. 5. (e) Log-likelihoods of fits to log energy differences, Eq. (B1). Red dashed line depicts goodness of fit for linear fits and the purple solid line is constructed for third-order polynomial fits. For $\phi \leq 0.65$, linear fits are as good as third-order fits. (f) p values for χ^2 statistics calculated for linear fits as a measure of quality of these fits. The panel shows that for none of the densities we can for sure reject the hypothesis that a fit is linear (p values are never below 0.05).

$$k_0 + k_1 \Sigma_p/N_{grp} + k_3 \Sigma_p^3/N_{grp}^3 = B + \Delta\alpha_p \Sigma_p + \Delta\kappa \Sigma_p^3. \text{ Hence } \Delta\alpha_p = k_1/N_{grp} \text{ and } \Delta\kappa = k_3/N_{grp}^3.$$

APPENDIX B: GOODNESS OF FIT FOR COMPRESSION ANGORICITY CALCULATION

Figure 9 presents goodness of fit data for log-differences linear fits of pressure angoricities (cf. Fig. 4).

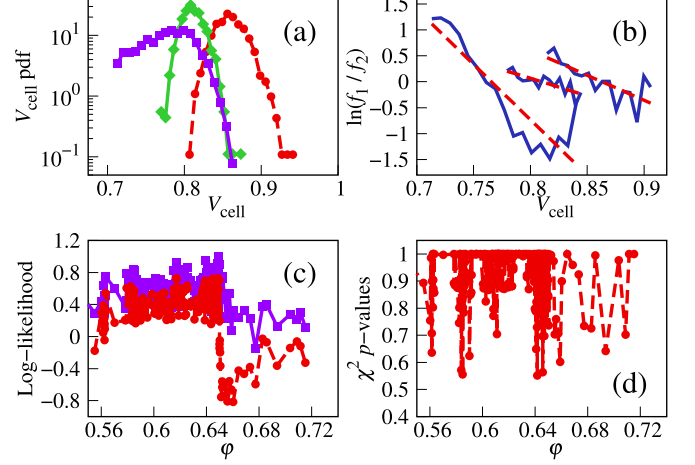


FIG. 11. Details of compactivity calculation. Panels (a)–(d) are equivalent to Figs. 3, 4, 9(a), and 9(b), respectively. (a) Probability distributions of Voronoi volumes per particle $V_{cell} = V_{grp}/N_{grp}$. Histograms are calculated for $M_{grp} \sim 1200$ subpackings (i.e., over $M_{grp} \sim 1200$ values of V_{grp}). Red dashed line (circles): $\phi = 0.605$; green solid line (diamonds): $\phi = 0.643$; and purple solid line (squares): $\phi = 0.669$. (b) Log energy differences for compactivity calculations from the overlapping histograms method, Eq. (14). For $\phi \lesssim 0.65$, the differences of logarithms look like straight lines, so the method of overlapping histograms is applicable. Left blue line: $\phi = 0.6685/0.6937$. Middle blue line: $\phi = 0.6430/0.6431$. Right blue line: $\phi = 0.6047/0.6082$. (c) Log-likelihoods of fits to log energy differences, Eq. (B1). Red dashed line depicts goodness of fit for linear fits and the purple solid line is constructed for third-order polynomial fits for log-differences. For $\phi \leq 0.65$, linear fits are as good as third-order fits. Contrary to angoricity plots, even third-order fit quality seems to deteriorate for $\phi > 0.65$. (f) p values for χ^2 statistics calculated for linear fits as a measure of quality of these fits. The panel shows that for none of the densities we can for sure reject the hypothesis that a fit is linear (p values are never below 0.05).

Figure 9(a) presents log-likelihoods of fits per bin under the assumption of independent and identically distributed (normally distributed) residuals,

$$l = \frac{1}{N_{bin}} \ln \left[\prod_{i=0}^{N_{bin}} \frac{1}{\sigma_{res} \sqrt{2\pi}} e^{-\frac{1}{2} \left(\frac{x_i - \mu_{res}}{\sigma_{res}} \right)^2} \right] = -\ln(\sigma_{res} \sqrt{2\pi}) - \frac{1}{N_{bin}} \frac{1}{2} \sum_{i=0}^{N_{bin}} \left(\frac{x_i - \mu_{res}}{\sigma_{res}} \right)^2, \quad (B1)$$

where N_{bin} is the number of bins for fitting the log-differences, σ_{res} is the standard deviation of residuals over the bins in the given fit, and μ_{res} is the mean of residuals. At each density, we present average values computed for a given packing over 10 histograms with other 10 packings at higher densities. Figure 9(a) presents two lines, the red dashed line depicts goodness of fit for linear fits and the purple solid line is constructed for third-order polynomial fits. Parabolic fits produce log-likelihoods between the two lines. This panel demonstrates that third-order fits have almost constant quality in the entire density range, while the quality of linear fits deteriorates at $\phi \sim 0.65$. Despite this, points with $\phi > 0.65$ match the same angoricity EOS as points with

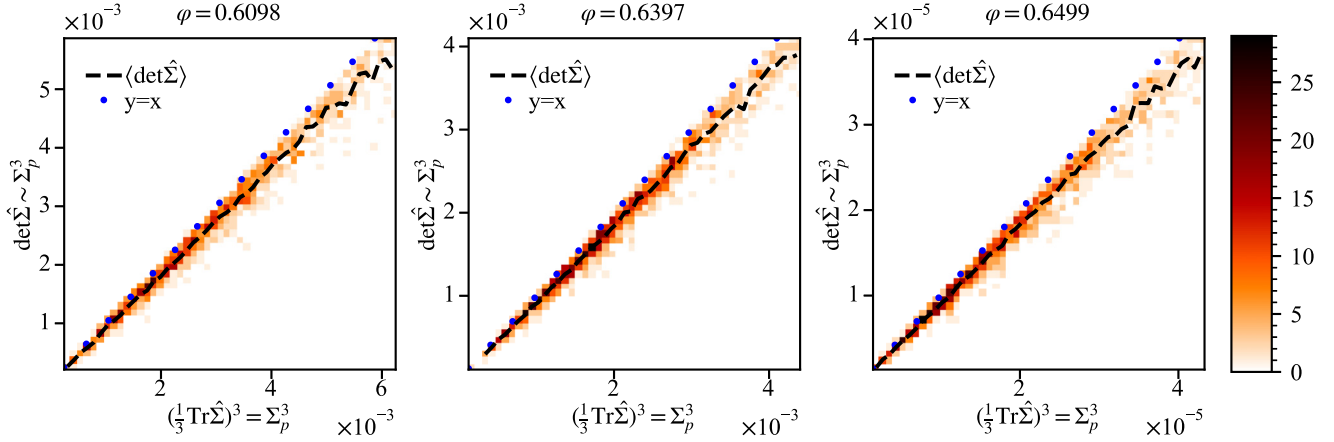


FIG. 12. Investigation of the applicability of using $\Sigma_p^3 = (\frac{1}{3}\text{Tr}\hat{\Sigma})^3$ instead of $\det \hat{\Sigma}$, i.e., of fitting histogram differences as one-dimensional curves with Eq. (20) instead of the full fit with a plane $B + \Delta\alpha_p \Sigma_p + \Delta\kappa \det \hat{\Sigma}$. For purely isotropic systems, we expect $\det \hat{\Sigma} = \det \Sigma_p I = \Sigma_p^3$, while for any systems by definition [Eq. (3)] $\frac{1}{3}\text{Tr}\hat{\Sigma} = \Sigma_p$. The simplified fit with Eq. (20) is applicable only when $\det \hat{\Sigma}$ is narrowly distributed around Σ_p^3 . The plots demonstrate the applicability of this assumption for three distinct packings with different densities. The panels present heat maps (2D histograms) of subpackings vs Σ_p^3 and $\det \hat{\Sigma}$. We take subpackings of eight particles, as used in the main text (~ 1200 subpackings per packing). Colors in each square cell represent the number of subpackings with values of Σ_p^3 and $\det \hat{\Sigma}$ inside narrow ranges corresponding to a cell. The colorbar maps colors to a number of particles in a cell. Black dashed lines represent mean values of $\det \hat{\Sigma}$ vs Σ_p^3 . They are very close to linear lines. Blue dots follow the line $\det \hat{\Sigma} = (\frac{1}{3}\text{Tr}\hat{\Sigma})^3$.

$\varphi \leq 0.65$, so we include them in the final plot Fig. 7(a) for A_p .

Figure 9(b) presents p values for χ^2 statistics calculated for linear fits as a measure of quality of these fits. It shows that for none of the densities we can for sure reject the hypothesis that a fit is linear (p values are never below 0.05).

APPENDIX C: DETAILS OF SHEAR ANGORICITY CALCULATION

This Appendix presents the details of shear angoricity calculations omitted in the main text. They are summarized in Fig. 10. Figures 10(a)–10(d) are equivalent to Figs. 3, 4, 1, and 5, respectively. Figures 10(e) and 10(f) are equivalent to Fig. 9(a) and Fig. 9(b). The results in Fig. 10 look quantitatively similar to the data for pressure angoricities.

APPENDIX D: DETAILS OF COMPACTIVITY CALCULATION

This Appendix along with Fig. 11 presents some details of compactivity calculations omitted in the main text. Figure 11(a) presents local energy distributions given that Voronoi volumes are granular energies. This panel is equivalent to Fig. 3 for pressure angoricity calculation. Figure 11(b) presents histogram differences in the log scale for Voronoi volumes. This figure is equivalent to Fig. 4 for angoricity calculation. Figures 11(c) and 11(d) present goodness of fit for log-difference fits.

APPENDIX E: DETAILS OF KERAMICITY CALCULATION

In this Appendix, we provide more details in Sec. VD for using higher-order fits for histogram log-differences and calculating keramicity.

Figure 12 demonstrates that it is justified to replace $\det \hat{\Sigma}$ with $a\Sigma_p^3$. It presents data for three packings at different densities, and in all of them $\det \hat{\Sigma}$ is very narrowly distributed around $a\Sigma_p^3$, with $a = 0.91$. We confirm that the same applies for all the packings in the range of densities $\varphi = 0.58$ – 0.65 . For packings in this range, $a = 0.89$ – 0.93 , so we can in fact use this range to fit histogram differences with a 1D curve Eq. (20) instead of using the full 2D fit Eq. (18). For $\varphi < 0.58$, a decreases below 0.89. For $\varphi > 0.65$, a also rapidly decreases (we omit the plot for brevity). For $\varphi > 0.65$, the distribution of $\det \hat{\Sigma}$ becomes wider as well, and for higher densities it becomes strongly nonlinear, presumably because the packings contain more and more crystalline inclusions.

Figure 12 also indicates why fitting with the full Eq. (18) would be error prone: Histogram differences in coordinates $\Sigma_p, \det \hat{\Sigma}$ follow a narrow curve $\Sigma_p, a\Sigma_p^3$, and the parameters of fitted planes have very high uncertainty, so the method of 1D fits with Eq. (19) is almost inevitable.

In the case that different packings would have different proportionality constant a , we could still use modified Eq. (20). If two packings had two proportionality constants a_1 and a_2 , then we would determine through histogram differences for them a cubic term $\kappa_1 a_1 - \kappa_2 a_2$, with both κ unknown. By setting κ_0 as an unknown constant for the very first packing in the sequence, we could determine all the values κ_i for all the packings iteratively, up until κ_0 . In our case, we do not need to use this more complicated scheme, because there exists a wide range of densities where $a \approx \text{const}$.

Figure 13 presents the results of using Eq. (20) for fitting histograms log-differences. Figure 13(a) presents inverse pressure angoricity estimates from these fits and corresponds to Fig. 4. It demonstrates that inverse pressure angoricity

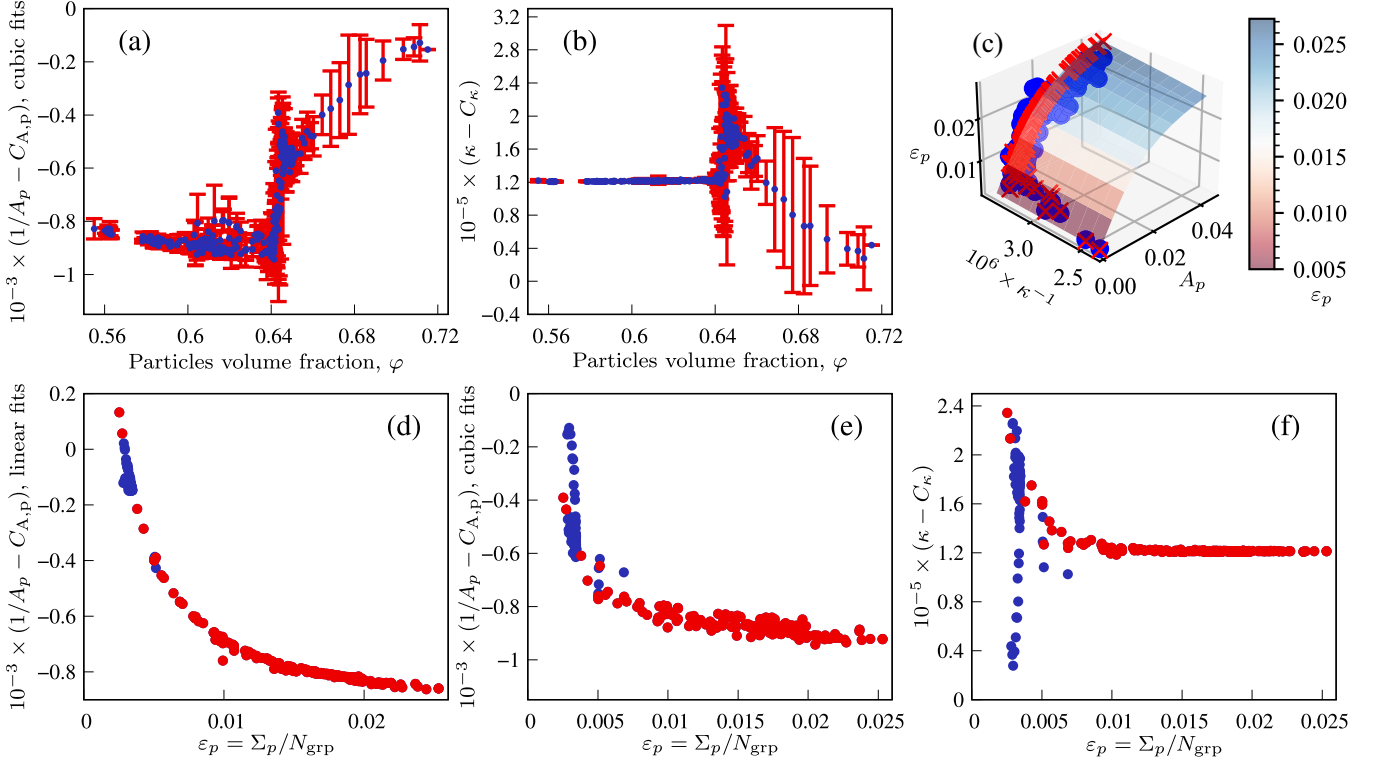


FIG. 13. Fitting histogram log-differences with higher-order fits (estimating keramicity), cf. Ref. [12] and Eq. (19). (a) Inverse pressure angoricities up to a constant when simultaneously estimating keramicities. This panel is equivalent to Fig. 5 but estimated from Eq. (20). The panel is qualitatively similar to Fig. 5. (b) Keramicity, or inverse “Beltrami volume temperature” [cf. Eq. (20)] up to an unknown constant. The error bars in panels (a) and (b) represent 3-sigma (97%) confidence intervals. (c) Complete angoricity-keramicity EOS [Eq. (22)] estimated from inverse angoricity and keramicity values from panels (a) and (b). Blue dots depict triples $(A_p, \kappa^{-1}, \langle \varepsilon_p \rangle)$, where $\varepsilon_p = \Sigma_p/N_{\text{grp}}$, determined from simulations for each granular packing. The surface represents the EOS from fitting Eq. (22), which can be interpreted as a 3D plot $\langle \varepsilon_p \rangle = f(A_p, \kappa^{-1})$. Figure 7(b) is a projection of this panel onto the axes $A_p, \langle \varepsilon_p \rangle$. (d) Inverse pressure angoricities up to a constant from a linear fit (13), keramicity not included, vs granular energy per particle $\varepsilon_p = \Sigma_p/N_{\text{grp}}$. Red circles are from packings with $\varphi \leq 0.644$; blue circles are points with $\varphi > 0.644$. The plot is a hyperbola and can indeed be fitted by Eq. (16). It shows that one can fit the data at all densities with the same Eq. (16), which we do in the main text, Fig. 7(a). (e) Same as panel (d) but with inverse angoricities from panel (a). (f) Keramicities up to a constant from panel (b) vs granular energy per particle $\varepsilon_p = \Sigma_p/N_{\text{grp}}$. Red circles are from packings with $\varphi \leq 0.644$; blue circles are points with $\varphi > 0.644$. Points from packings with $\varphi \leq 0.644$ seem to lie on the same curve, meaning they can be fitted with Eq. (22). The plot shows that packings with $\varphi > 0.644$ do not comply with a EOS, presumably because keramicity is more sensitive to packings having a random structure, so we exclude them from fitting keramicity EOS [cf. panel (c) and Fig. 7(b)].

estimates from Eq. (20) are qualitatively close to the ones from Fig. 4. Confidence intervals are wider, though, because we are using higher-order fits.

Figure 13(b) depicts the estimates of κ up to an unknown constant C_κ . The plateau in the values to the left is explained as follows: As Figs. 4 and 9 hint, histogram log-differences for $\varphi \gtrsim 0.65$ are almost linear, and higher-order terms for fitting them are small. Hence, $\Delta\kappa$ is close to zero for $\varphi \lesssim 0.65$, and $\kappa - C_\kappa$ is almost constant. Still, it is very remarkable that small changes in $\kappa - C_\kappa$, as well as $\frac{1}{A_p} - C_{A,p}$, can match large differences in granular energies from Fig. 1 after final EOS fits in Fig. 7.

Figure 13(c) presents the complete pressure angoricity-inverse keramicity EOS Eq. (22) estimated from inverse pressure angoricity and keramicity values found in Figs. 13(a) and 13(b). Blue dots depict triples $(A_p, \kappa^{-1}, \langle \varepsilon_p \rangle)$, where $\varepsilon_p = \Sigma_p/N_{\text{grp}}$ as determined from simulations for each granular packing. The surface represents the EOS fit (22), which can be interpreted as a 3D plot $\langle \varepsilon_p \rangle = f(A_p, \kappa^{-1})$. Figure 7(b) is

a projection of this figure onto the axes $A_p, \langle \varepsilon_p \rangle$, because A_p has much stronger impact on $\langle \varepsilon_p \rangle$.

Figures 13(d)–13(f) provide an analysis in which range we can reasonably fit angoricities and compactivities. Figure 13(d) shows that the data for inverse pressure angoricity determined from linear fits to histogram log-differences [no keramicity, Eq. (13)] look consistent (hyperbolic) in the entire range of φ and we can fit all the data with the same EOS (15), which we do in the main text [Fig. 7(a)]. For comparison, we provide in panel (e) an equivalent plot for $\frac{1}{A_p} - C_{A,p}$ from cubic fits (19). Blue points correspond to $\varphi > 0.644$. Figure 13(f) provides data for $\kappa - C_\kappa$ vs $\langle \Sigma_p \rangle/N_{\text{grp}}$. It clearly shows that points at $\varphi > 0.644$ deviate from the curve at $\varphi \leq 0.644$, presumably because keramicity is more sensitive to how random packing structure is. Given that the data for keramicity clearly deviates from a simple curve at $\varphi = 0.644$, we exclude points at $\varphi > 0.644$ from fitting the linear EOS for pressure angoricities as well [Figs. 13(e) and 13(f)].

APPENDIX F: FINITE-SIZE EFFECTS

In this Appendix, we investigate finite-size effects on angoricity measurements. We repeated the measurements that we did in the main text with different group sizes, $N_{\text{grp}} = 7, 8, 12, 16,$ and 32 , i.e., calculated granular energy histograms, calculated log-differences of histograms, estimated inverse temperatures, and fitted the EOS coefficient $k_{A,p}$ from Eq. (16).

To avoid potentially using data where the statistical theory might not apply, we used only data points in the range $\varphi \leq 0.65$ for EOS estimation, where the packings are random. It slightly increases confidence intervals for the $k_{A,p}$ estimates.

Figure 14 presents the corresponding measurements and extrapolation to the thermodynamic limit $N_{\text{grp}} \rightarrow \infty$. We represent the finite-size dependence in the form $k_{A,p} = f(1/N_{\text{grp}}^2)$ and fit the data with the second-order polynomial, i.e., $k_{A,p} = a + b\frac{1}{N_{\text{grp}}^2} + c\frac{1}{N_{\text{grp}}^4}$. The error bars denote 95% confidence intervals. The estimate of $k_{A,p}$ in the thermodynamic limit $N_{\text{grp}} \rightarrow \infty$ is $k_{A,p} = 2.60 \pm 0.27$. When using a simpler form, a parabolic fit over $1/N_{\text{grp}}k_{A,p} = a + b\frac{1}{N_{\text{grp}}} + c\frac{1}{N_{\text{grp}}^2}$, the result is 2.459 ± 0.61 (not shown for brevity).

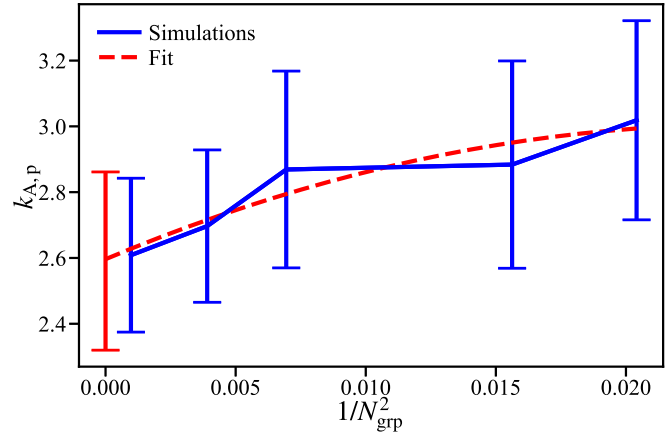


FIG. 14. Analysis of finite-size effects on the granular EOS for pressure angoricity. We repeated the measurements from the main text to estimate $k_{A,p}$ from Eq. (16) for different group sizes of sub-packings, $N_{\text{grp}} = 7, 8, 12, 16,$ and 32 . All the results for different group sizes look qualitatively similar to the results presented in the main text. We fitted this curve in the form $k_{A,p} = f(1/N_{\text{grp}}^2)$, where f is the second-order polynomial. The estimate of $k_{A,p}$ in the thermodynamic limit $N_{\text{grp}} \rightarrow \infty$ is $k_{A,p} = 2.60 \pm 0.27$. The error bars represent 95% confidence intervals.

- [1] D. Bi, S. Henkes, K. E. Daniels, and B. Chakraborty, The statistical physics of athermal materials, *Annu. Rev. Condens. Matter Phys.* **6**, 63 (2015).
- [2] A. Baule, F. Morone, H. J. Herrmann, and H. A. Makse, Edwards statistical mechanics for jammed granular matter, *Rev. Mod. Phys.* **90**, 015006 (2018).
- [3] G. Parisi and F. Zamponi, Mean-field theory of hard sphere glasses and jamming, *Rev. Mod. Phys.* **82**, 789 (2010).
- [4] S. Torquato and F. H. Stillinger, Jammed hard-particle packings: From Kepler to Bernal and beyond, *Rev. Mod. Phys.* **82**, 2633 (2010).
- [5] S. F. Edwards, The full canonical ensemble of a granular system, *Physica A* **353**, 114 (2005).
- [6] R. Blumenfeld and S. F. Edwards, On granular stress statistics: Compactivity, angoricity, and some open issues, *J. Phys. Chem. B* **113**, 3981 (2009).
- [7] S. Henkes and B. Chakraborty, Statistical mechanics framework for static granular matter, *Phys. Rev. E* **79**, 061301 (2009).
- [8] C. Song, P. Wang, and H. A. Makse, A phase diagram for jammed matter, *Nature (London)* **453**, 629 (2008).
- [9] K. Wang, C. Song, P. Wang, and H. A. Makse, Angoricity and compactivity describe the jamming transition in soft particulate matter, *Europhys. Lett.* **91**, 68001 (2010).
- [10] J. G. Puckett and K. E. Daniels, Equilibrating temperaturelike variables in jammed granular subsystems, *Phys. Rev. Lett.* **110**, 058001 (2013).
- [11] E. S. Bililign, J. E. Kollmer, and K. E. Daniels, Protocol dependence and state variables in the force-moment ensemble, *Phys. Rev. Lett.* **122**, 038001 (2019).
- [12] Y. Wu and S. Teitel, Maximum entropy and the stress distribution in soft disk packings above jamming, *Phys. Rev. E* **92**, 022207 (2015).
- [13] E. DeGiuli, Edwards field theory for glasses and granular matter, *Phys. Rev. E* **98**, 033001 (2018).
- [14] Y. Yuan, Y. Xing, J. Zheng, Z. Li, H. Yuan, S. Zhang, Z. Zeng, C. Xia, H. Tong, W. Kob, J. Zhang, and Y. Wang, Experimental test of the edwards volume ensemble for tapped granular packings, *Phys. Rev. Lett.* **127**, 018002 (2021).
- [15] P. A. Kelly, *Mechanics Lecture Notes: Foundations of Continuum Mechanics* (University of Auckland, Auckland, 2013).
- [16] D. S. Dean and A. Lefèvre, Possible test of the thermodynamic approach to granular media, *Phys. Rev. Lett.* **90**, 198301 (2003).
- [17] S.-C. Zhao and M. Schröter, Measuring the configurational temperature of a binary disc packing, *Soft Matter* **10**, 4208 (2014).
- [18] B. D. Lubachevsky and F. H. Stillinger, Geometric properties of random disk packings, *J. Stat. Phys.* **60**, 561 (1990).
- [19] B. D. Lubachevsky, How to simulate billiards and similar systems, *J. Comput. Phys.* **94**, 255 (1991).
- [20] V. Baranau and U. Tallarek, Random-close packing limits for monodisperse and polydisperse hard spheres, *Soft Matter* **10**, 3826 (2014).
- [21] V. Baranau and U. Tallarek, Another resolution of the configurational entropy paradox as applied to hard spheres, *J. Chem. Phys.* **147**, 224503 (2017).
- [22] V. Baranau, <https://www.github.com/VasiliBaranov/packing-generation/>.
- [23] P. Wang, C. Song, Y. Jin, and H. A. Makse, Jamming II: Edwards' statistical mechanics of random packings of hard spheres, *Physica A* **390**, 427 (2011).
- [24] C. Briscoe, C. Song, P. Wang, and H. A. Makse, Jamming III: Characterizing randomness via the entropy of jammed matter, *Physica A* **389**, 3978 (2010).
- [25] H. Makse, <https://hmake.cny.cuny.edu/software-and-data/>.

- [26] V. Baranau, D. Hlushkou, S. Khirevich, and U. Tallarek, Pore-size entropy of random hard-sphere packings, *Soft Matter* **9**, 3361 (2013).
- [27] B. P. Tighe, A. R. T. van Eerd, and T. J. H. Vlugt, Entropy maximization in the force network ensemble for granular solids, *Phys. Rev. Lett.* **100**, 238001 (2008).
- [28] B. P. Tighe and T. J. H. Vlugt, Force balance in canonical ensembles of static granular packings, *J. Stat. Mech.* (2010) P01015.
- [29] B. P. Tighe and T. J. H. Vlugt, Stress fluctuations in granular force networks, *J. Stat. Mech.* (2011) P04002.
- [30] C. S. O'Hern, L. E. Silbert, A. J. Liu, and S. R. Nagel, Jamming at zero temperature and zero applied stress: The epitome of disorder, *Phys. Rev. E* **68**, 011306 (2003).
- [31] L. Berthier and T. A. Witten, Glass transition of dense fluids of hard and compressible spheres, *Phys. Rev. E* **80**, 021502 (2009).
- [32] V. Baranau and U. Tallarek, On the jamming phase diagram for frictionless hard-sphere packings, *Soft Matter* **10**, 7838 (2014).
- [33] V. Baranau and U. Tallarek, How to predict the ideal glass transition density in polydisperse hard-sphere packings, *J. Chem. Phys.* **143**, 044501 (2015).
- [34] M. Bargiel and E. M. Tory, Packing fraction and measures of disorder of ultradense irregular packings of equal spheres. II. Transition from dense random packing, *Adv. Powder Technol.* **12**, 533 (2001).
- [35] K. Lochmann, L. Oger, and D. Stoyan, Statistical analysis of random sphere packings with variable radius distribution, *Solid State Sci.* **8**, 1397 (2006).
- [36] B. A. Klumov, S. A. Khrapak, and G. E. Morfill, Structural properties of dense hard sphere packings, *Phys. Rev. B* **83**, 184105 (2011).
- [37] S. C. Kapfer, W. Mickel, K. Mecke, and G. E. Schroder-Turk, Jammed spheres: Minkowski tensors reveal onset of local crystallinity, *Phys. Rev. E* **85**, 030301(R) (2012).
- [38] B. A. Klumov, Y. Jin, and H. A. Makse, Structural properties of dense hard sphere packings, *J. Phys. Chem. B* **118**, 10761 (2014).
- [39] V. Baranau, S.-C. Zhao, M. Scheel, U. Tallarek, and M. Schröter, Upper bound on the Edwards entropy in frictional monodisperse hard-sphere packings, *Soft Matter* **12**, 3991 (2016).
- [40] V. Baranau and U. Tallarek, Correct use of excess configurational entropies to study the ideal glass transition in hard-sphere systems with continuous polydispersity, *AIP Adv.* **12**, 085204 (2022).